Remarkably Weak Anisotropy in Thermal Conductivity of Two-Dimensional Hybrid Perovskite Butylammonium Lead Iodide Crystals

Chen Li[1‡], Hao Ma[1‡], Tianyang Li[2], Jinghang Dai[1], Md Abu Jafar Rasel[3], Alessandro Mattoni[4],

Ahmet Alatas[5], Malcolm G. Thomas[6], Zachary W. Rouse[7], Avi Shragai[8], Shefford P. Baker[7], Brad

Ramshaw[8], Joseph P. Feser[3], David B. Mitzi[2], and Zhiting Tian[1]*

[1]Sibley School of Mechanical and Aerospace Engineering, Cornell University, Ithaca, NY

14853, USA

[2]Department of Mechanical Engineering & Materials Science, Duke University, Durham, NC

27708, USA

[3]Department of Mechanical Engineering, University of Delaware, Newark, DE 19716, USA

[4]Istituto Officina dei Materiali (CNR-IOM) Cagliari, SLACS, Cittadella Universitaria, I-09042

Monserrato, (CA), Italy

[5]Advanced Photon Source, Argonne National Laboratory, Argonne, Illinois 60439, USA
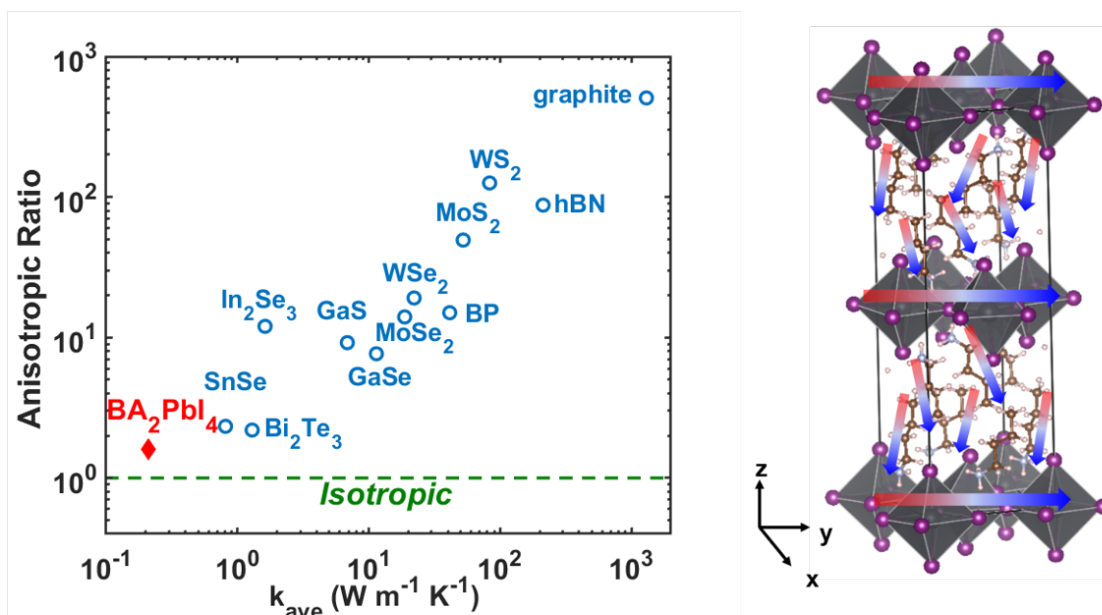
[6]Cornell Center for Materials Research, Cornell University, Ithaca, New York 14853, USA

[7]Department of Materials Science and Engineering, Cornell University, Ithaca, New York 14853, USA

[8]Laboratory of Atomic and Solid State Physics, Cornell University, Ithaca, New York 14853, USA

ABSTRACT

Two-dimensional (2D) hybrid organic-inorganic perovskites consisting of alternating organic and inorganic layers are a new class of layered structures. They have attracted increasing interest for photovoltaic, optoelectronic, and thermoelectric applications, where knowing their thermal transport properties is critical. We carry out both experimental and computational studies on thermal transport properties of 2D butylammonium lead iodide crystals and find their thermal conductivity is ultralow (below $0.3 \ \mathrm{W \ m^{-1} \ K^{-1}}$) with very weak anisotropy (around 1.5) among layered crystals. Further analysis reveals that the unique structure with the preferential alignment of organic chains and complicated energy landscape leads to moderately smaller phonon lifetimes in the out-of-plane direction and comparable phonon group velocities in in-plane and out-of-plane directions. These new findings may guide the future design of novel hybrid materials with desired thermal conductivity for various applications.

MAIN TEXT

Two-dimensional (2D) hybrid organic-inorganic perovskites have emerged as promising candidates for solar cells[1], light-emitting diodes[2], and photodetectors[3], and thermoelectrics[4], due to their significantly improved ambient stability[5], remarkable structural flexibility, and tunability of physical properties[6] compared with their three-dimensional (3D) counterparts. Understanding the thermal transport in 2D hybrid perovskites is important for the thermal management and energy conversion efficiency in optoelectronic and thermoelectric applications. The unique 2D-layered structures with alternating organic and inorganic layers could potentially differentiate their thermal

transport properties from other conventional 2D-layered structures. Despite very recent reports[7–9] on the ultralow out-of-plane thermal conductivity ($k_\perp$), our knowledge about thermal transport in 2D hybrid perovskites is scarce. The anisotropy in the thermal conductivity remains unknown due to the lack of in-plane thermal conductivity ($k_\parallel$). Moreover, to obtain deep insights into underlying mechanisms, a close look at lattice dynamics and phonon properties in 2D hybrid perovskites is needed but difficult to obtain, given the complex crystal structure and complicated energy landscape.

In this work, we perform a comprehensive study on the thermal conductivity and phonon properties in butylammonium lead iodide BA_2PbI_4 ($BA = C_4H_9NH_3^+$) at room temperature. The 2D BA_2PbI_4 hybrid perovskite consists of bilayers of interdigitated $C_4H_9NH_3^+$ cations alternating with inorganic PbI_4^{2-} layers.[10] The 2D layers are held together by weak vdW/electrostatic interactions. We choose BA_2PbI_4 as the example material because it has a surge in popularity with studies on its mechanical[11], electrical[12], and optical[13] properties. Despite challenges in measuring $k_\parallel$ of small thin crystals, we are able to measure $k_\parallel$ by transient thermal grating (TTG) technique. The measured $k_\parallel$'s of two independent sets of BA_2PbI_4 crystals are 0.28 ± 0.01 W m^{-1} K^{-1} and 0.29 ± 0.01 W m^{-1} K^{-1}, respectively. The $k_\perp$ of BA_2PbI_4 crystalline thin films was found to be 0.18 ± 0.04 W m^{-1} K^{-1} by time-domain thermoreflectance (TDTR) measurement at the room temperature[7]. A slightly lower value of $k_\perp = 0.125 \pm 0.089$ W m^{-1} K^{-1} was obtained for BA_2PbI_4 single crystal by TDTR at 330 K[8], probably due to the laser heating induced structural rearrangements at 325 K. Using molecular dynamics (MD), our calculated $k_\parallel$ and $k_\perp$ of 0.27 ± 0.01 W m^{-1} K^{-1} and 0.18 ± 0.01 W m^{-1} K^{-1} at the room temperature agree very well with the experimental data. Most strikingly, the 2D layered BA_2PbI_4 crystals exhibit incredibly weak

anisotropy in their thermal conductivity. The anisotropic ratio ($k_{\parallel}/k_{\perp}$) is exceptionally small compared to other layered crystals and even approaches the isotropic limit. To gain a microscopic picture, we further map out the phonon dispersion of BA_2PbI_4 using inelastic x-ray (IXS) measurements and the spectral energy density (SED) calculations. This is the first study on phonon dispersion of a 2D hybrid material. We build the relationship between the crystal structure features and the phonon characteristics to understand its weak anisotropy in the thermal conductivity. The weak vdW/electrostatic interactions among organic chains and at organic-inorganic interfaces lead to moderately smaller phonon lifetimes in the out-of-plane direction and the preferential orientation of the organic chains results in comparable phonon group velocities, giving slightly smaller $k_{\perp}$.

Results

Crystal characterization

We carefully prepare two sets of high-quality BA_2PbI_4 crystals (sample #1 and #2, Figure 1a) using a slow cooling method[14] (see Supporting Information (SI) for details) in two independent groups to cross-check the results. Sample #1 has a crystal size up to 5 mm in the in-plane direction and an out-of-plane thickness around 200 μm, while sample #2 has a crystal size up to 2.5 mm in the in-plane direction and an out-of-plane thickness ranging from 200 μm to 550 μm. The x-ray diffraction (XRD) measurements of samples #1 and #2 (Figure 1b) show sharp (00l) peaks equidistant in 2θ, which demonstrates the high degree of crystallinity along the out-of-plane direction. The crystal structure obtained from single-crystal XRD (SC-XRD) can be found in SI. In order to create smooth sample surfaces for TTG measurement, we exfoliate the samples using Scotch tape. The sample roughness can be significantly reduced through exfoliation as

5

demonstrated by atomic force microscopy (AFM) examination (Figure 1c). The scanning electron microscope (SEM) images in Figure 1d further verify the smooth surface after exfoliation and show the clear layered features at the sample edges. The SEM images with a larger scale bar can be found in SI and no obvious grains are observed in large areas along the in-plane direction.
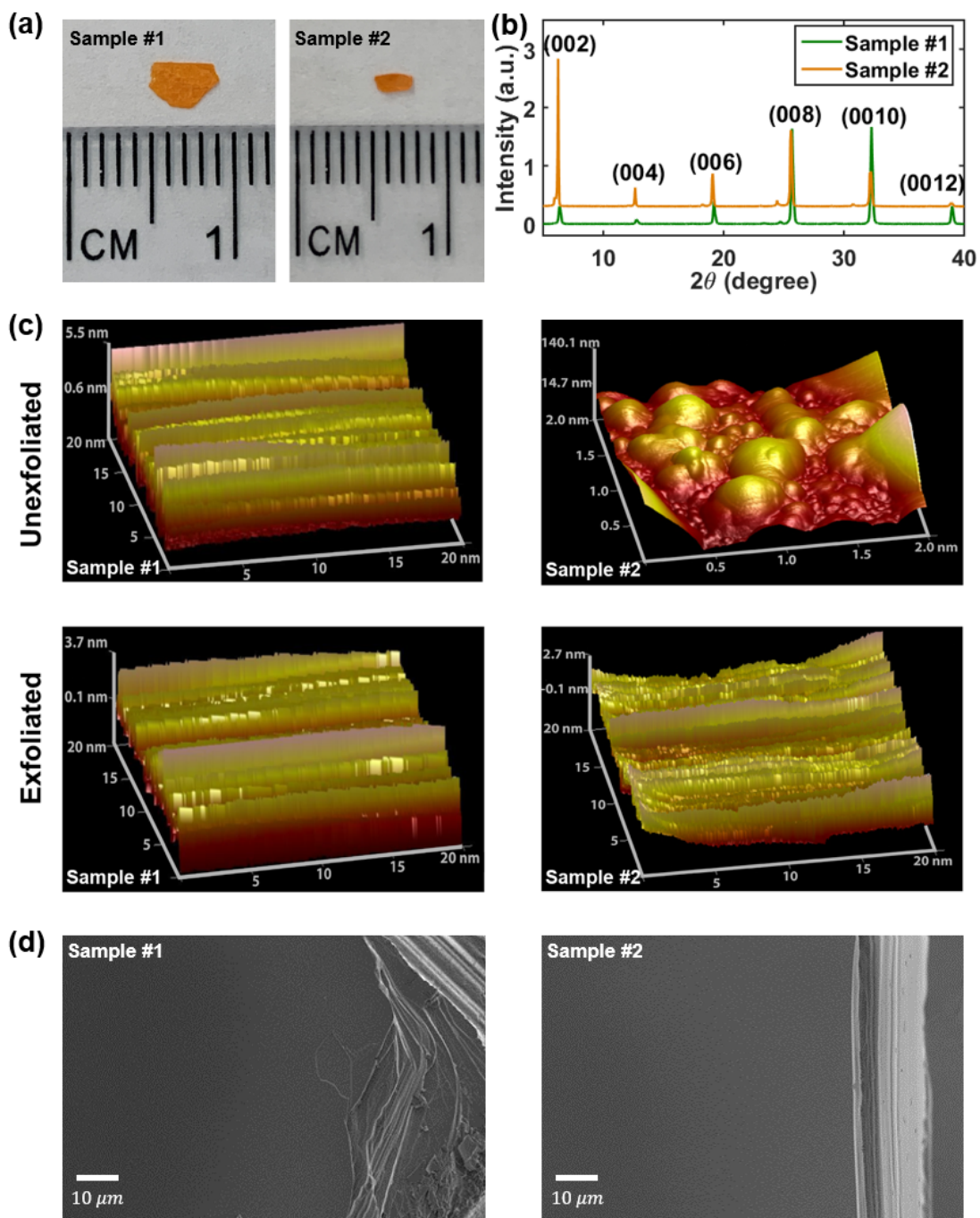
Figure 1 (a) Images of synthesized samples #1 and sample #2. (b) the XRD pattern of samples #1 and #2 measured by using Cu Kα radiation. (c) AFM image of unexfoliated and exfoliated samples. The surface roughness of sample #1 is reduced from R_q=1.51 nm to R_q=0.89 nm, and the surface

roughness of sample #2 from R_q=33.60 nm to R_q=0.77 nm after exfoliation. Note that R_q is the root mean square average of height deviations taken from the mean image data plane. The difference in initial surface roughness between samples #1 and #2 results from the different synthesis parameters. (d) SEM images of the top surface for exfoliated samples.

Thermal conductivity measurements and calculations

We then perform TTG measurements (see SI for experimental details) on those two sets of samples. TTG is a non-contact optical technique[15–17], allowing highly accurate in-plane measurements of thin films. The in-plane thermal diffusivity is determined by fitting the thermal decay data as in Figure 2a. Using a specific heat capacity of 0.48 J $g^{-1}K^{-1}$ measured by differential scanning calorimetry (DSC) method and a density of 2.68 g cm^{-3} determined by SC-XRD (see SI for details), we extract the in-plane thermal conductivity of samples #1 and #2 to be 0.28 ± 0.01 W m^{-1} K^{-1} and 0.29 ± 0.01 W m^{-1} K^{-1}, respectively, at 300 K. We are unable to reliably extract the out-of-plane thermal conductivity of these single crystals using frequency domain thermoreflectance (FDTR) mainly due to the low sensitivity and laser heating, as also confirmed by a latest publication[9]. Therefore, we compare the in-plane thermal conductivity of BA_2PbI_4 crystals measured by TTG with the out-of-plane thermal conductivity of BA_2PbI_4 thin film measured by TDTR[7]. Although TDTR and TTG are two different techniques, the measured samples in both experiments are fully crystalline, and the measured results agree well with calculation. We think the comparison between the in-plane and out-of-plane thermal conductivities is fair and the best we could do with the existing techniques.
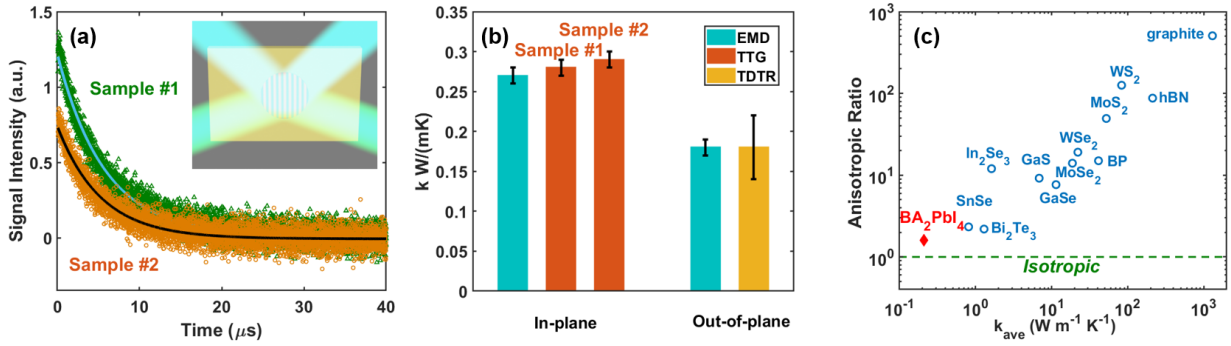
Figure 2 (a) The obtained thermal decay data from TTG measurements. Green triangles and orange circles denote samples #1 and #2, respectively. Blue and black curves denote the fittings from the theoretical thermal model of samples #1 and #2, respectively. Inset is a schematic of the pump beams (blue) forming thermal gratings on samples and the probe beam (green) diffracting from the thermal gratings and overlapping with a reference beam (green) in TTG measurement. (b) In-plane ($k_\parallel$) and out-of-plane ($k_\perp$) thermal conductivity of 2D BA_2PbI_4 hybrid perovskite crystals at 300 K. Orange, yellow and blue denote the thermal conductivity of crystals measured by TTG in this study, crystalline thin films measured using TDTR[7], and single crystal calculated from EMD simulations in this study, respectively. (c) The anisotropic ratio ($k_\parallel/k_\perp$) vs. average thermal conductivity (k_{ave}) of BA_2PbI_4 crystals and other layered single crystals[18–23].

We calculate the thermal conductivity of 2D BA_2PbI_4 using equilibrium MD (EMD) simulations with a classical model potential for the hybrid perovskite (MYP) force field[24]. We choose the MYP force field because it successfully reproduced the structural, elastic, vibrational properties[25], and thermal conductivity[26] of 3D $MAPbI_3$ (MA = $CH_3NH_3^+$). In addition, the MYP force field was applied to calculate the molar heat capacity of BA_2PbI_4 [7] and the result agrees well with our DSC measurements. The predicted $k_\parallel$ and $k_\perp$ of BA_2PbI_4 are 0.27 ± 0.01 W m^{-1} K^{-1} and 0.18 ± 0.01

W m^{-1} K^{-1} at 300 K, respectively. The in-plane and out-of-plane thermal conductivities of BA$_2$PbI$_4$ predicted by EMD simulations with MYP force field are in good agreement with the TTG and TDTR measurements, respectively (Figure 2b).

The average thermal conductivity of BA$_2$PbI$_4$ is 0.21 W m^{-1} K^{-1}, which is comparable to most amorphous polymers and much lower than other layered crystal structures (Figure 2c). Moreover, it is smaller than the thermal conductivity of 3D MAPbI$_3$ (0.3 - 0.5 W m^{-1} K^{-1})[27–29], and comparable to that of "0D" MA$_3$Bi$_2$I$_9$ (0.23 W m^{-1} K^{-1})[30]. This can be intuitively explained by the strength of interactions. MAPbI$_3$ has a 3D continuous inorganic framework of strong Pb-I ionic/covalent bonds, while MA$_3$Bi$_2$I$_9$ has discontinuous inorganic units separated by organic units and 2D BA$_2$PbI$_4$ has alternating inorganic/organic layers held together by weak long-range electrostatic and vdW interactions. Similar to other hybrid perovskites[30,31], the ultralow thermal conductivity of BA$_2$PbI$_4$ can be attributed to low phonon group velocities resulting from ultralow phonon frequencies and short phonon lifetimes originating from a significant overlap between acoustic and optical phonons as indicated by its phonon dispersion from IXS measurements (See SI for experimental details) and SED calculations in Figure 3a. The low phonon group velocities are further supported by ultralow indentation moduli from nanoindentation measurements and the speed of sound measurements by pulse echo technique. The detailed discussion can be found in SI.

Anisotropic thermal conductivity analysis

Most strikingly, the anisotropic ratio of BA$_2$PbI$_4$ crystal is only 1.50 from EMD calculations and 1.58 from experimental measurements, which are much lower than other layered crystals and approach the isotropic limit as shown in Figure 2c. To understand the exceptionally small

10

anisotropy, we take a close look at the structure and phonon properties. Note that the organic chains are preferentially aligned in the out-of-plane direction in BA_2PbI_4 (Figure 3b). In the in-plane direction, there are strong intraplanar Pb-I ionic/covalent bonds in the inorganic layers and weak vdW/electrostatic interchain interactions in the organic layers. In the out-of-plane direction, there are covalent bonds (C-C and C-N) within organic chains and weak vdW/electrostatic interactions between organic chains (there are two chains stacking vertically in each layer) and at organic-inorganic interfaces.

Thermal conductivity can be expressed as a function of the volumetric heat capacity C_v, average phonon group velocity $\bar{v}$, and phonon lifetime $\bar{\tau}$ as $k = \frac{1}{3}C_v\bar{v}^2\bar{\tau}$. We then connect their structure features to phonon lifetimes and group velocities. In the in-plane direction, the $PbI_4{}^{2-}$ framework allows for continuous heat conduction pathways (Figure 3b). In other words, within the inorganic layers, phonons have relatively large lifetimes. In contrast, the heat conduction path along the out-of-plane direction is interrupted by the weak interchain interactions and organic-inorganic interfaces (Figure 3b), and phonons can be strongly scattered at those joints. Strong anharmonicity at the organic-inorganic interfaces also contributes to phonon scatterings and suppress phonon lifetimes in the out-of-plane direction[26,32–34]. The smaller phonon lifetimes along the out-of-plane direction are supported by phonon dispersion using the SED method (see SI for details). The broader the phonon dispersion curves, the smaller the phonon lifetimes[35]. As shown in Figure 3a, acoustic phonon branches in the **Γ-Z** direction are more blurred than that in the **Γ-X/Y** directions, indicating smaller phonon lifetimes along the out-of-plane direction. By further extracting the widths of SED peaks, we reach the same conclusion, as shown in Figure S11. This difference is not significant, though, due to the small volume fraction of the inorganic layers. In brief, the

phonon lifetimes are relatively anisotropic mainly because of the continuous heat conduction path in the inorganic framework along the in-plane direction vs. the disconnected pathways in the out-of-plane direction.

For phonon group velocities, they are related to the strength of the interatomic interactions. The preferential alignment of the organic chain is the key factor that balances out the weak interlayered interactions. The orientation of the organic chains was reported to have a large effect on the out-of-plane thermal conductivity of 2D hybrids.[7] Here, we pin down the orientational effects to phonon group velocities. Since stronger covalent bonds in one crystal axis result in higher group velocities in that axis[36], the group velocities along the organic chain direction are higher than those perpendicular to the chain direction. In the out-of-plane direction, the preferentially vertical alignment of organic chains leads to large phonon group velocities along the organic chains, compensating the weak interlayered interactions and resulting in similar phonon group velocities to the in-plane direction. In the in-plane direction, despite the strong intraplanar P-I ionic/covalent bonds in the inorganic PbI_4^{2-} framework, the organic layers have weak vdW/electrostatic interactions and take up a large volume fraction of 78%. This dwarfs the average bonding strength and, thus, the overall phonon group velocities. In brief, the interplay among different effects leads to comparable group velocities between in-plane and out-of-plane directions. This is supported by the group velocities obtained from the phonon dispersion in Figure 3a and our estimations on bond strength comparison between in-plane and out-of-plane directions (see details in SI). As a result, moderately smaller phonon lifetimes along the out-of-plane direction and the comparable group velocities between in-plane and out-of-plane directions give slightly smaller $k_\perp$ and thus remarkably weak anisotropy.
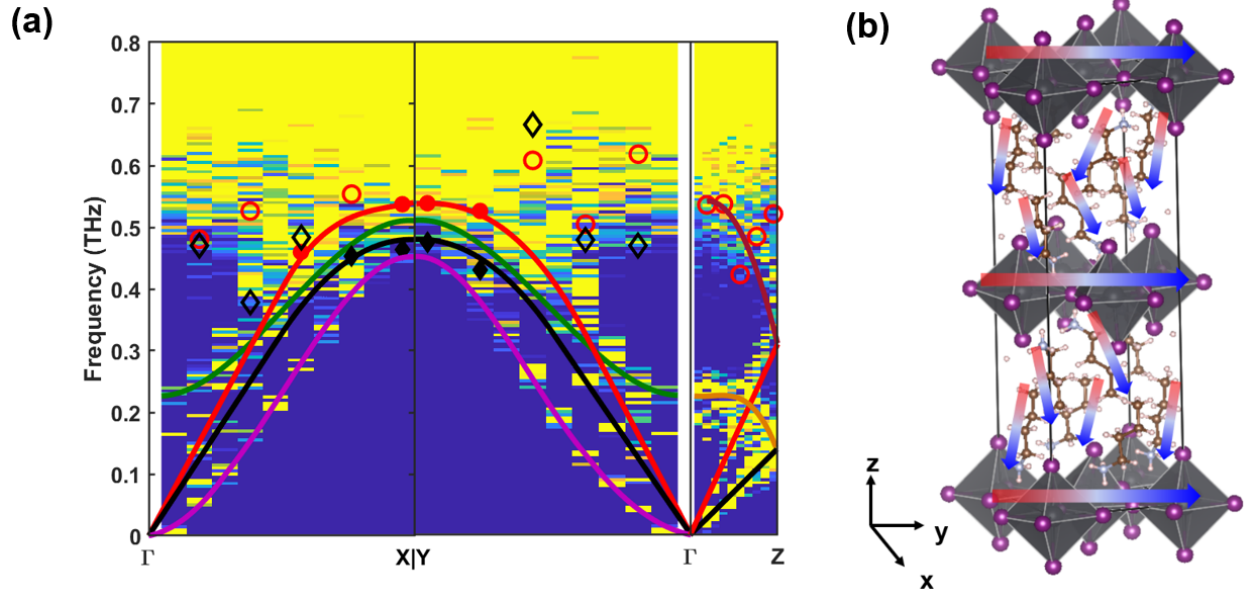
12

Figure 3 (a) Phonon dispersion of BA$_2$PbI$_4$ single crystal measured by IXS and calculated by SED at 300 K. The high symmetry points are chosen based on the first Brillouin zone of a simple orthorhombic lattice: **Γ** (0 0 0), **X** (0.5 0 0), **Y**(0 0.5 0), and **Z** (0 0 0.5) in the units of **b$_1$**=($\frac{2\pi}{a}$, 0, 0), **b$_2$**=(0, $\frac{2\pi}{b}$, 0), **b$_3$**=(0, 0, $\frac{2\pi}{c}$). The markers represent phonons measured by IXS. Red solid circles, black solid diamonds, red circles, black diamonds denote longitudinal acoustic (LA) modes, transverse acoustic (TA) modes, longitudinal-optical (LO) modes, and transverse-optical (TO) modes, respectively. The red (LA), black (TA), magenta (ZA), green (ZO), orange (TO), and maroon (LO) lines were drawn based on the calculated phonon dispersion by SED. Phonon modes by IXS and SED are in good agreement. Note that our calculated directions (Γ-X: (X 0.05 0) Γ-Y: (0.05 Y 0)) are not exactly along high symmetric lines ((Γ-X: (X 0 0) Γ-Y: (0 Y 0))) since the SED calculations are based on a 20×20×1 supercell and an even larger supercell is too computationally expensive. The calculated Γ-Z is along the high symmetric line. (b) The unit cell of 2D BA$_2$PbI$_4$

13

single crystal with arrows denoting preferential heat conduction paths along both in-plane and out-of-plane directions.

Conclusion

In summary, we perform TTG and IXS measurements, along with MD simulations to investigate the thermal transport properties of 2D BA_2PbI_4 crystals at 300 K. Despite the anisotropic crystalline structure, we find its thermal conductivity is amorphous-polymer-like with the anisotropic ratio approaching the isotropic limit. Further analysis reveals that the weak anisotropy comes from the comparable phonon group velocities and moderately different phonon lifetimes in the in-plane and out-of-plane directions. The continuous inorganic PbI_4^{2-} framework with strong intraplanar Pb-I ionic/covalent bonds in the framework forms favorable heat conduction paths along the in-plane direction, while the weak vdW/electrostatic interactions among organic chains and at organic-inorganic interfaces lead to strong phonon scatterings and thus smaller phonon lifetimes along the out-of-plane direction. The preferential orientations of organic $C_4H_9NH_3^+$ chains in the out-of-plane direction and the large volume fraction of the organic layers results in comparable phonon group velocities between the out-of-plane and in-plane directions. The fundamental insights obtained in this study can advance the understanding of 2D hybrid perovskites and guide the rational design of materials with desired thermal conductivity for optoelectronic and thermoelectric applications.

ASSOCIATED CONTENT

Supporting Information

Crystal Synthesis; XRD measurements and Crystal Structure; TTG measurements; Specific heat capacity measurements; Mechanical Properties; IXS measurements; EMD simulations; SED Method; Phonon Dispersion Analysis; Phonon group velocity; additional figures.

AUTHOR INFORMATION

Corresponding Author

*Email: zhiting@cornell.edu

Author Contributions

‡Both authors (C.L. and H.M.) contributed equally to this work. C.L., H.M., and Z.T. conceived the study. T.L. and D.M. synthesized sample #2 and conducted SC-XRD on single crystals used in IXS and powder XRD on crystals used in TTG measurements. J.D. assisted with TTG measurements. M.R. and J.F. synthesized samples #1 and conducted XRD and DSC measurements on sample #1. A.S. and B. R. performed the pulse echo measurements. A.M. provided the MYP force field. Z.W. and S.B. assisted with the nanoindentation measurements. M.T. assisted with the SEM measurements. A.A. assisted with the IXS measurements. The manuscript was written through contributions of all authors. The authors declare no competing interests.

15

REFERENCES

(1)   Zhang, F.; Lu, H.; Tong, J.; Berry, J. J.; Beard, M. C.; Zhu, K. Advances in Two-Dimensional Organic–Inorganic Hybrid Perovskites. *Energy Environ. Sci.* **2020**, *13* (4), 1154–1186.

(2)   Yuan, M.; Quan, L. N.; Comin, R.; Walters, G.; Sabatini, R.; Voznyy, O.; Hoogland, S.; Zhao, Y.; Beauregard, E. M.; Kanjanaboos, P. Perovskite Energy Funnels for Efficient Light-Emitting Diodes. *Nat. Nanotechnol.* **2016**, *11* (10), 872–877.

(3)   Leng, K.; Abdelwahab, I.; Verzhbitskiy, I.; Telychko, M.; Chu, L.; Fu, W.; Chi, X.; Guo, N.; Chen, Z.; Chen, Z. Molecularly Thin Two-Dimensional Hybrid Perovskites with Tunable Optoelectronic Properties Due to Reversible Surface Relaxation. *Nat. Mater.* **2018**, *17* (10), 908–914.

(4)   Haque, M. A.; Kee, S.; Villalva, D. R.; Ong, W.; Baran, D. Halide Perovskites: Thermal Transport and Prospects for Thermoelectricity. *Adv. Sci.* **2020**, *7* (10), 1903389.

(5)   Smith, I. C.; Hoke, E. T.; Solis-Ibarra, D.; McGehee, M. D.; Karunadasa, H. I. A Layered Hybrid Perovskite Solar-cell Absorber with Enhanced Moisture Stability. *Angew. Chemie Int. Ed.* **2014**, *53* (42), 11232–11235.

(6)   Saparov, B.; Mitzi, D. B. Organic–Inorganic Perovskites: Structural Versatility for Functional Materials Design. *Chem. Rev.* **2016**, *116* (7), 4558–4596.

(7)   Giri, A.; Chen, A. Z.; Mattoni, A.; Aryana, K.; Zhang, D.; Hu, X.; Lee, S.-H.; Choi, J. J.; Hopkins, P. E. Ultralow Thermal Conductivity of Two-Dimensional Metal Halide Perovskites. *Nano Lett.* **2020**, *20* (5), 3331–3337.

(8)   Rasel, M. A. J.; Giri, A.; Olson, D. H.; Ni, C.; Hopkins, P. E.; Feser, J. P. Chain-Length Dependence of Thermal Conductivity in 2D Alkylammonium Lead Iodide Single Crystals. *ACS Appl. Mater. Interfaces* **2020**, *12* (48), 53705–53711.

(9)   Christodoulides, A. D.; Guo, P.; Dai, L.; Hoffman, J. M.; Li, X.; Zuo, X.; Rosenmann, D.; Brumberg, A.; Kanatzidis, M. G.; Schaller, R. D. Signatures of Coherent Phonon Transport in Ultralow Thermal Conductivity Two-Dimensional Ruddlesden–Popper Phase Perovskites. *ACS Nano* **2021**, *15* (3), 4165–4172.

(10)   Mitzi, D. B. Synthesis, Crystal Structure, and Optical and Thermal Properties of (C4H9NH3) 2MI4 (M= Ge, Sn, Pb). *Chem. Mater.* **1996**, *8* (3), 791–800.

(11)   Tu, Q.; Spanopoulos, I.; Hao, S.; Wolverton, C.; Kanatzidis, M. G.; Shekhawat, G. S.; Dravid, V. P. Out-of-Plane Mechanical Properties of 2D Hybrid Organic-Inorganic Perovskites by Nanoindentation. *ACS Appl. Mater. Interfaces* **2018**, *10* (26), 22167–22173.

https://doi.org/10.1021/acsami.8b05138.

(12)   Ma, L.; Dai, J.; Zeng, X. C. Two-Dimensional Single-Layer Organic-Inorganic Hybrid Perovskite Semiconductors. *Adv. Energy Mater.* **2017**, *7* (7), 1601731. https://doi.org/10.1002/aenm.201601731.

(13)   Yin, T.; Liu, B.; Yan, J.; Fang, Y.; Chen, M.; Kiang Chong, W.; Jiang, S.; Kuo, J.-L.; Fang, J.; Liang, P.; Wei, S.; Ping Loh, K.; Chien Sum, T.; White, T. J.; Xiang Shen, Z. Pressure-Engineered Structural and Optical Properties of Two-Dimensional (C 4 H 9 NH 3) 2 PbI 4 Perovskite Exfoliated Nm-Thin Flakes. *J. Am. Chem. Soc* **2019**, *141*, 1235–1241. https://doi.org/10.1021/jacs.8b07765.

(14)   Billing, D. G.; Lemmerer, A. Synthesis, Characterization and Phase Transitions in the Inorganic–Organic Layered Perovskite-Type Hybrids [(CnH2n+ 1NH3) 2PbI4], N= 4, 5 and 6. *Acta Crystallogr. Sect. B Struct. Sci.* **2007**, *63* (5), 735–747.

(15)   Johnson, J. A.; Maznev, A. A.; Bulsara, M. T.; Fitzgerald, E. A.; Harman, T. C.; Calawa, S.; Vineis, C. J.; Turner, G.; Nelson, K. A. Phase-Controlled, Heterodyne Laser-Induced Transient Grating Measurements of Thermal Transport Properties in Opaque Material. *J. Appl. Phys.* **2012**, *111* (2), 23503.

(16)   Johnson, J. A.; Maznev, A. A.; Cuffe, J.; Eliason, J. K.; Minnich, A. J.; Kehoe, T.; Torres, C. M. S.; Chen, G.; Nelson, K. A. Direct Measurement of Room-Temperature Nondiffusive Thermal Transport Over Micron Distances in a Silicon Membrane. *Phys. Rev. Lett.* **2013**, *110* (2). https://doi.org/10.1103/PhysRevLett.110.025901.

(17)   Li, C.; Ma, Y.; Tian, Z. Thermal Switching of Thermoresponsive Polymer Aqueous Solutions. *ACS Macro Lett.* **2017**, 53–58. https://doi.org/10.1021/acsmacrolett.7b00938.

(18)   McKinney, R.; Gorai, P.; Toberer, E. S.; Stevanovic, V. Rapid Prediction of Anisotropic Lattice Thermal Conductivity: Application to Layered Materials. *Chem. Mater.* **2019**, *31* (6), 2048–2057.

(19)   Jiang, P.; Qian, X.; Yang, R.; Lindsay, L. Anisotropic Thermal Transport in Bulk Hexagonal Boron Nitride. *Phys. Rev. Mater.* **2018**, *2* (6), 64005.

(20)   Jiang, P.; Qian, X.; Gu, X.; Yang, R. Probing Anisotropic Thermal Conductivity of Transition Metal Dichalcogenides MX2 (M= Mo, W and X= S, Se) Using Time-Domain Thermoreflectance. *Adv. Mater.* **2017**, *29* (36), 1701068.

(21)   Jang, H.; Wood, J. D.; Ryder, C. R.; Hersam, M. C.; Cahill, D. G. Anisotropic Thermal Conductivity of Exfoliated Black Phosphorus. *Adv. Mater.* **2015**, *27* (48), 8017–8022.

(22)   Hsin, C.-L.; Huang, J.-H.; Spiewak, P.; Ciupiński, Ł.; Lee, S.-W. Anisotropy of Thermal Conductivity in In2Se3 Nanostructures. *Appl. Surf. Sci.* **2019**, *494*, 867–870.

(23)   Kang, J. S.; Wu, H.; Li, M.; Hu, Y. Intrinsic Low Thermal Conductivity and Phonon Renormalization Due to Strong Anharmonicity of Single-Crystal Tin Selenide. *Nano Lett.* **2019**, *19* (8), 4941–4948. https://doi.org/10.1021/acs.nanolett.9b01056.

(24)   Mattoni, A.; Filippetti, A.; Saba, M. I.; Delugas, P. Methylammonium Rotational Dynamics in Lead Halide Perovskite by Classical Molecular Dynamics: The Role of Temperature. *J.*

Phys. Chem. C **2015**, *119* (30), 17421–17428.

(25)   Mattoni, A.; Filippetti, A.; Saba, M. I.; Caddeo, C.; Delugas, P. Temperature Evolution of Methylammonium Trihalide Vibrations at the Atomic Scale. *J. Phys. Chem. Lett.* **2016**, *7* (3), 529–535.

(26)   Caddeo, C.; Melis, C.; Saba, M. I.; Filippetti, A.; Colombo, L.; Mattoni, A. Tuning the Thermal Conductivity of Methylammonium Lead Halide by the Molecular Substructure. *Phys. Chem. Chem. Phys.* **2016**, *18* (35), 24318–24324.

(27)   Ye, T.; Wang, X.; Li, X.; Yan, A. Q.; Ramakrishna, S.; Xu, J. Ultra-High Seebeck Coefficient and Low Thermal Conductivity of a Centimeter-Sized Perovskite Single Crystal Acquired by a Modified Fast Growth Method. *J. Mater. Chem. C* **2017**, *5* (5), 1255–1260. https://doi.org/10.1039/c6tc04594d.

(28)   Pisoni, A.; Jaćimović, J.; Barišić, O. S.; Spina, M.; Gaál, R.; Forró, L.; Horváth, E. Ultra-Low Thermal Conductivity in Organic-Inorganic Hybrid Perovskite CH3NH3PbI3. *J. Phys. Chem. Lett.* **2014**, *5* (14), 2488–2492. https://doi.org/10.1021/jz5012109.

(29)   Elbaz, G. A.; Ong, W. L.; Doud, E. A.; Kim, P.; Paley, D. W.; Roy, X.; Malen, J. A. Phonon Speed, Not Scattering, Differentiates Thermal Transport in Lead Halide Perovskites. *Nano Lett.* **2017**, *17* (9), 5734–5739. https://doi.org/10.1021/acs.nanolett.7b02696.

(30)   Ma, H.; Li, C.; Ma, Y.; Wang, H.; Rouse, Z. W.; Zhang, Z.; Slebodnick, C.; Alatas, A.; Baker, S. P.; Urban, J. J. Supercompliant and Soft (CH 3 NH 3) 3 Bi 2 I 9 Crystal with Ultralow Thermal Conductivity. *Phys. Rev. Lett.* **2019**, *123* (15), 155901.

(31)   Ma, H.; Ma, Y.; Wang, H.; Slebodnick, C.; Alatas, A.; Urban, J. J.; Tian, Z. Experimental Phonon Dispersion and Lifetimes of Tetragonal CH3NH3PbI3 Perovskite Crystals. *J. Phys. Chem. Lett.* **2018**, *10* (1), 1–6.

(32)   Guo, P.; Stoumpos, C. C.; Mao, L.; Sadasivam, S.; Ketterson, J. B.; Darancet, P.; Kanatzidis, M. G.; Schaller, R. D. Cross-Plane Coherent Acoustic Phonons in Two-Dimensional Organic-Inorganic Hybrid Perovskites. *Nat. Commun.* **2018**, *9* (1), 1–9.

(33)   Li, D.; McGaughey, A. J. H. Phonon Dynamics at Surfaces and Interfaces and Its Implications in Energy Transport in Nanostructured Materials—an Opinion Paper. *Nanoscale Microscale Thermophys. Eng.* **2015**, *19* (2), 166–182.

(34)   Ong, W.-L.; O'Brien, E. S.; Dougherty, P. S. M.; Paley, D. W.; Higgs III, C. F.; McGaughey, A. J. H.; Malen, J. A.; Roy, X. Orientational Order Controls Crystalline and Amorphous Thermal Transport in Superatomic Crystals. *Nat. Mater.* **2017**, *16* (1), 83–88.

(35)   Ma, H.; O'Donnel, E.; Tian, Z. Tunable Thermal Conductivity of π-Conjugated Two-Dimensional Polymers. *Nanoscale* **2018**, *10* (29), 13924–13929.

(36)   Cheng, P.; Shulumba, N.; Minnich, A. J. Thermal Transport and Phonon Focusing in Complex Molecular Crystals: Ab Initio Study of Polythiophene. *Phys. Rev. B* **2019**, *100* (9), 94306.

Supporting Information

Remarkably Weak Anisotropy in Thermal Conductivity of Two-Dimensional Hybrid Perovskite Butylammonium Lead Iodide Crystals

Chen Li[1][‡], Hao Ma[1][‡], Tianyang Li[2], Jinghang Dai[1], Md Abu Jafar Rasel[3], Alessandro Mattoni[4], Ahmet Alatas[5], Malcolm G. Thomas[6], Zachary W. Rouse[7], Avi Shragai[8], Shefford P. Baker[7], Brad Ramshaw[8], Joseph P. Feser[3], David B. Mitzi[2], and Zhiting Tian[1]*

[1]Sibley School of Mechanical and Aerospace Engineering, Cornell University, Ithaca, NY 14853, USA

[2]Department of Mechanical Engineering & Materials Science, Duke University, Durham, NC 27708, USA

[3]Department of Mechanical Engineering, University of Delaware, Newark, DE 19716, USA

[4]Istituto Officina dei Materiali (CNR-IOM) Cagliari, SLACS, Cittadella Universitaria, I-09042 Monserrato, (CA), Italy

[5]Advanced Photon Source, Argonne National Laboratory, Argonne, Illinois 60439, USA

[6]Cornell Center for Materials Research, Cornell University, Ithaca, New York 14853, USA

[7]Department of Materials Science and Engineering, Cornell University, Ithaca, New York 14853, USA

[8]Laboratory of Atomic and Solid State Physics, Cornell University, Ithaca, New York 14853, USA

Crystal Synthesis

Sample #1

The synthesis of BA_2PbI_4 crystals (sample #1) follows the slow cooling method reported previously[1]. 0.47 mmol PbI_2 and 1 mmol butylamine are added into 3 ml of 47 wt% hydroiodic acid solution. The resulting precipitate is dissolved by refluxing for 2 hours at 100 ^{o}C. The solution is then cooled at 2 °C/hour to room temperature to induce slow precipitation and crystal growth. The orange crystals are removed and rinsed with hexane over a filter to remove reagents, and then placed in a desiccator for 2 hours to complete the drying process. Suitable crystals are selected for nanoindentation, speed of sound, and thermal conductivity measurements. Samples are stored in a glove box while not performing measurements to be on the safe side.

Sample #2

BA_2PbI_4 crystals (sample #2) are also synthesized from the slow cooling method. 0.2 mmol PbI_2, 0.4 mmol butylamine, and 0.1 mL hypophosphorous acid are added into 1mL of 57 wt% hydroiodic acid. The solution is heated up to 95 ℃ to dissolve all solids and then slowly cooled down to room temperature over 96 hours. The orange crystals are then separated by filtration and washed using ethyl ether with yield ~55%. Suitable crystals are selected for SC-XRD, IXS,

nanoindentation, and thermal conductivity measurements. Samples are stored in a glove box while not performing measurements to be on the safe side.
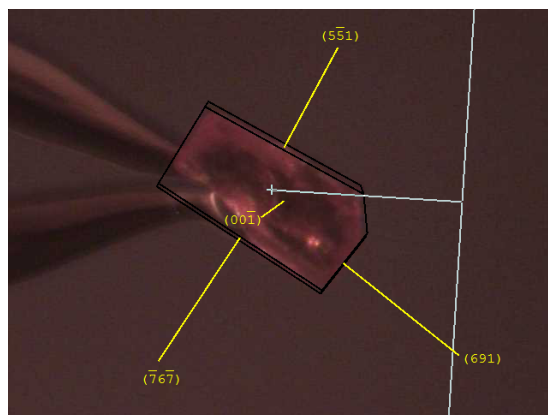

Figure S1. Image of BA_2PbI_4 single crystal for IXS measurements.

The image of BA_2PbI_4 single crystal chosen from sample #2 used in IXS measurements is shown in Figure S1. The SEM images in Figure S2 show the large smooth area of BA_2PbI_4 crystals used in TTG measurements. No obvious grains are observed in large areas along the in-plane direction.
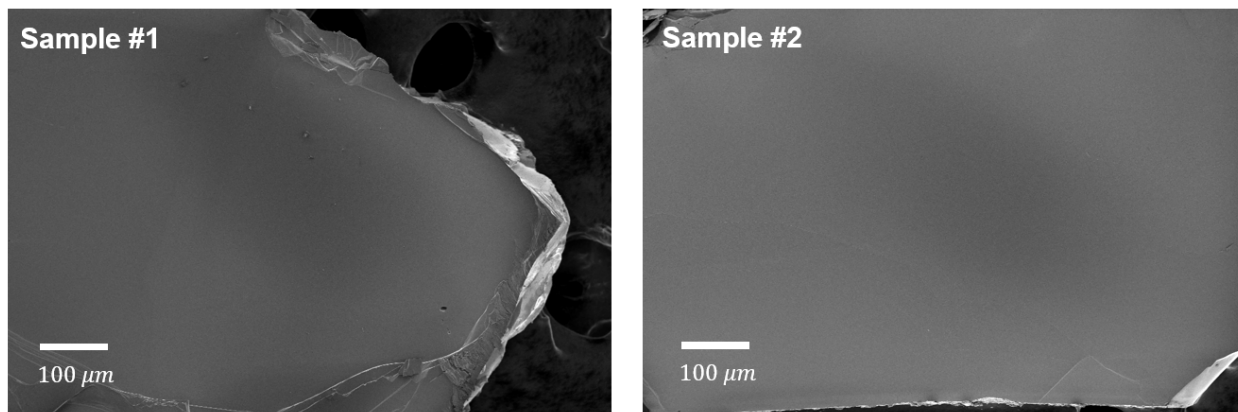

Figure S2. SEM images of BA_2PbI_4 crystals for TTG measurements.

XRD measurements and Crystal Structure

XRD patterns of sample #1 and #2 in Figure 1d are collected at room temperature from the Bruker D8 instrument (Cu Kα radiation) and the Rigaku SmartLab X-Ray Diffractometer (Cu Kα radiation), respectively. Reflections associated with (001) planes (l=2,4,5,6,8,10,12) are visible, confirming that the samples are single crystal in the out-of-plane direction and the crystals strongly favor growth where the layers orient parallel to the substrate. The associated interplanar spacings closely match previous reports for the corresponding orthorhombic phases[1,2]. Note that the unmarked side peaks may result from a twin or crack in the crystals.

SC-XRD measurements are performed on a selected crystal on the Bruker D8 instrument, all at room temperature using Mo Kα radiation (= 0.71073 Å). The crystal structure is solved and refined using the Olex2 program[3] and Shelx software package[4]. The data collection is set up to achieve >99.5% coverage and an average redundancy from >3.5 to 0.8 Å assuming Pmmm Laue symmetry. The multi-scan absorption correction is applied. No twin law is detected and applied in the refinements. The obtained structure unit cell is shown in Figure S3. Crystal data and structure refinement for BA_2PbI_4 single crystal are listed in Table S1.
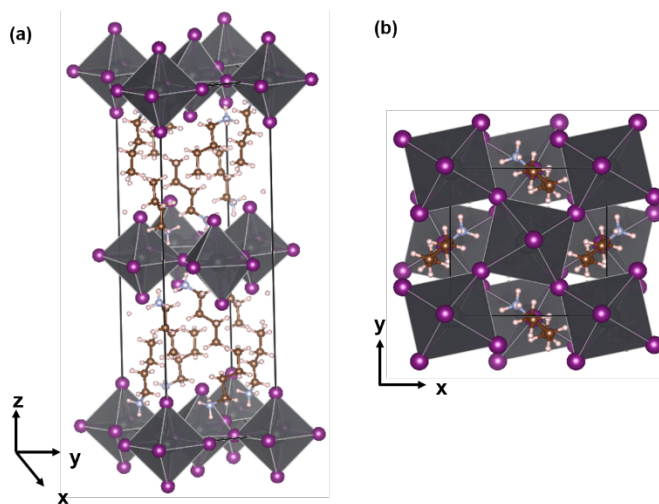

Figure S3 (a) Top view and (b) side view of BA_2PbI_4 unit cell.

Table S1. Crystal data and structure refinement for BA_2PbI_4 single crystal used in IXS measurements.

Compound name	BA_2PbI_4
Empirical formula	$C_8H_{24}N_2I_4Pb$
Formula weight	839.14
Crystal size (mm)	$0.068 \times 0.191 \times 0.224$
Space group	Pbca
T / K	296
λ / Å	0.71073
a / Å	8.8810(2)
b / Å	8.6999(2)
c / Å	27.6251(8)
α / °	90
β / °	90
γ / °	90
V / Å^3	2134.42(9)
Z	4
Density / g·cm^{-3}	2.684
μ / mm^{-1}	13.671
$F(000)$	1425
θ for data collection	3.956-26.430
Measured refls.	13342
Independent refls.	2303
Observed reflection ($I > 2\sigma(I)$)	1832
Peak and hole / e Å^{-3}	0.863/-1.195
R_{int}	0.0329
No. of parameters	72
GOF	1.298
$^aR_1, wR_2$ [$I > 2\sigma(I)$]	0.0429, 0.0859
$^aR_1, wR_2$ (all data)	0.0552, 0.0893

Powder XRD measurements for BA_2PbI_4 crystal used in TTG measurements (sample #2) are carried out on a PANalytical Empyrean Powder x-ray diffractometer using Cu Kα radiation, with x-ray tube operating condition at 45 kV and 40 mA. The powder XRD pattern of BA_2PbI_4 crystal

(sample #2) used in TTG measurements as shown in Figure S4 matches the calculated XRD patterns and shows that the crystal has a pure phase.
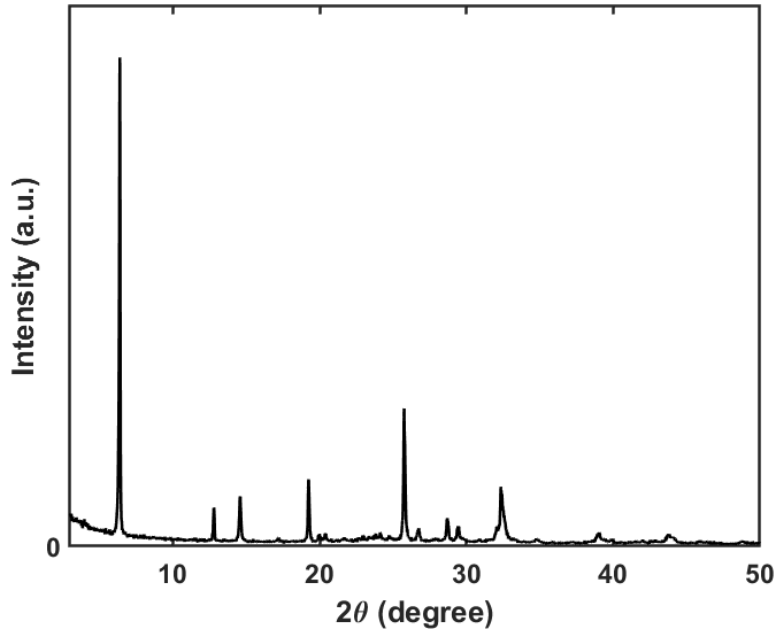

Figure S4. Powder XRD pattern of BA_2PbI_4 crystals (sample #2) used in TTG measurements.

TTG measurements

A full description of TTG can be found in prior work[5-7]. Our TTG setup is shown in Figure S5. A picosecond Nd:YVO4 laser (pulse duration 2 ps, wavelength λ_e= 517 nm, frequency 1 kHz, energy 0.02 μJ per pulse) is used for excitation. An electro-optically gated beam from a continuous-wave (CW) solid-state laser (wavelength λ_p = 532 nm, CW power 1 mW, chopped at 10% duty cycle with an effective power of 0.1 mW) is used as the probe beam. The horizontally polarized excitation beam and the vertically polarized probe beam are focused onto the mask. To image the mask pattern onto the sample, we use spherical lenses with focal distances f_1 = 15 cm and f_2 = 10 cm. In the sample, the laser spot diameters are about 50 μm for the excitation pulses, probe and

reference beams. The heterodyne phase is controlled with a motorized actuator by adjusting the angle of a glass plate. The diffracted signal combined with a reference beam, which is derived from the same source and attenuated by a neutral density filter (ND-3), is detected by a balanced amplified photodetector (bandwidth 45 MHz) whose output is recorded with an oscilloscope (4 GHz bandwidth). TTG measurements of reflection geometry are performed on suspended BA_2PbI_4 crystals at the grating period $L = 6.64\ \mu m$.

The temperature grating decay at the surface can be written as in Equation (S1) [5]

$$T(z = 0, x, t) = A(\alpha_z t)^{-1/2} \cos(qx) \exp\left(-\alpha_x q^2 t\right) \tag{S1}$$

where x is the grating dimension, z is the depth into the material, t is the time, T is the deviation from equilibrium temperature, q is the grating wavevector, α_z is the out-of-plane thermal diffusivity, and α_x is the in-plane thermal diffusivity. The initial part of the decay signal helps determine out-of-plane thermal diffusivity. However, we fit the decay signal after 100 ns to extract only the in-plane thermal diffusivity and to avoid the potential contributions from the excited carrier diffusion. The decay signal adequately follows a single exponential decay curve. The in-plane thermal conductivity is then obtained from the in-plane thermal diffusivity together with the density ρ and the specific heat capacity C_p as in Equation (S2)

$$k_\parallel = \rho C_p \alpha_x \tag{S2}$$

As shown in Figure S6, TTG signal intensity at a given spot of BA_2PbI_4 crystals has minimal variation within the initial 20 seconds after the lasers are on. We measure each spot of the crystals within 10 seconds after turning on the lasers to minimize the radiation damage on the crystals.
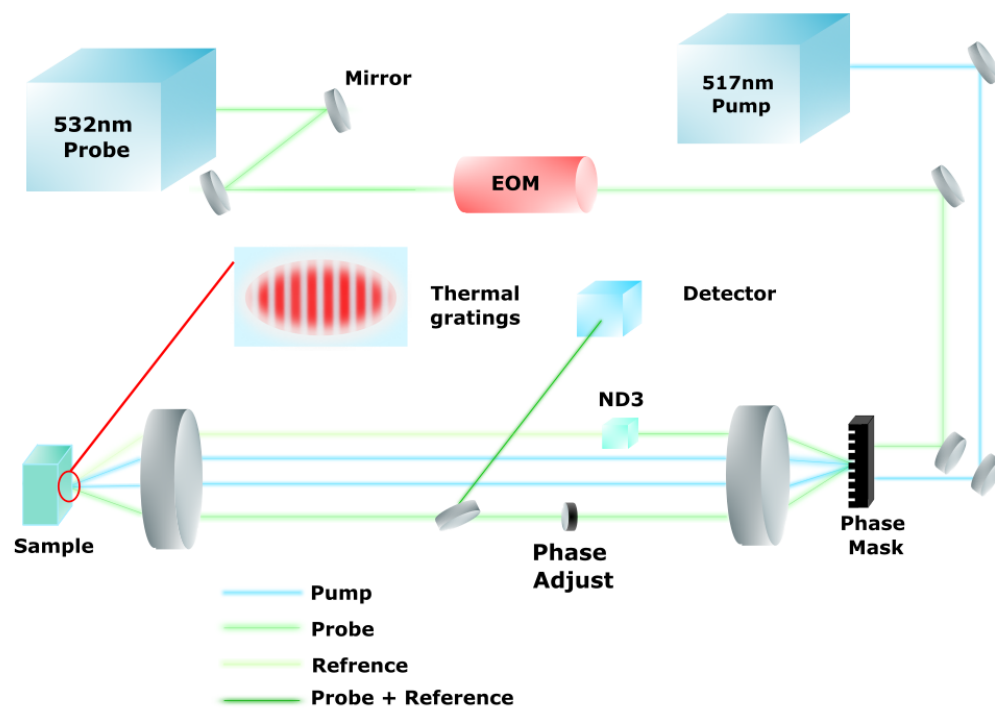
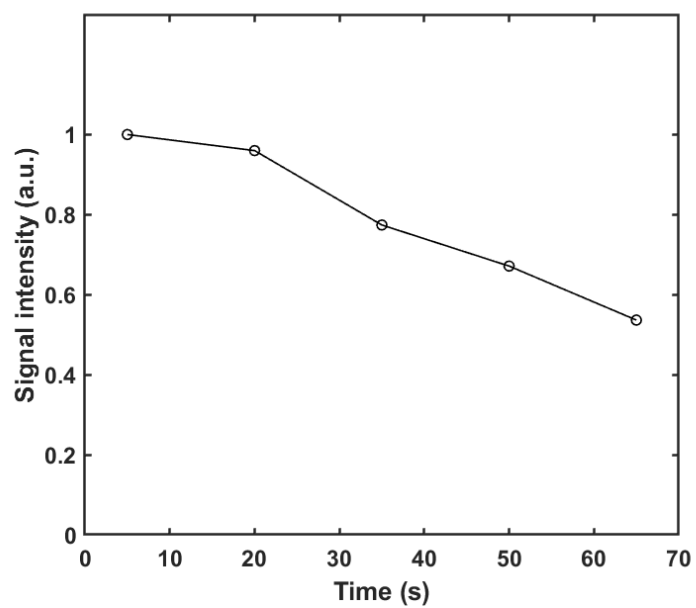**Figure S5.** Schematic of TTG system.

Figure S6. Signal intensity during the TTG measurements at a given spot of BA_2PbI_4 crystals as a function of time after turning on the lasers.

Specific heat capacity measurements

BA_2PbI_4 crystals (sample #1) are heated in DSC from 193 K to 373 K with a ramp rate of 20 K/min in a hermetic aluminum pan. As the thermogravimetric analysis shows that crystals start losing weight after 493 K, we keep temperature-dependent specific heat capacity measurement below this temperature. DSC results show that this crystal has two phases within the measurement temperature. The endothermic upward peak around 280 K corresponds to phase transition and the small peak around 320 K could be due to sample movement during measurement or minor structural rearrangements in the crystals. BA_2PbI_4 has an orthorhombic structure in both phases and phase transition from orthorhombic (I) to orthorhombic (II) is primarily to the movement of the essentially rigid butylammonium cations relative to the inorganic layers[1].

The specific heat capacity of BA_2PbI_4 is determined from DSC using the 3-run heat capacity method (ASTM E1269) where three separate DSC measurements, i) dual empty pans, ii) a sapphire in a pan vs. a reference pan, and iii) the sample in a pan vs a reference pan, are combined to obtain the temperature-dependent specific heat capacity as in Figure S7. The specific heat capacity at 300 K is determined to be $0.48\ \mathrm{J\,g^{-1}K^{-1}}$.
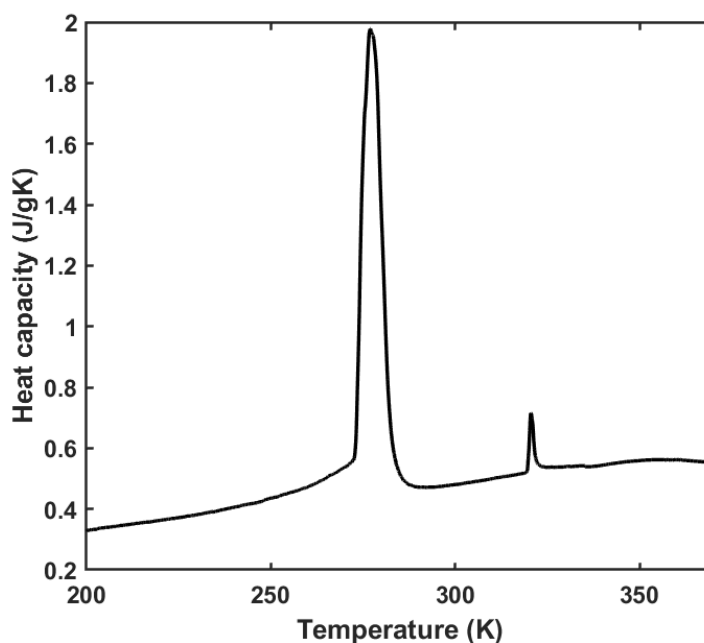
Figure S7. Temperature-dependent specific heat capacity of BA_2PbI_4 from DSC measurement.

Mechanical Properties

Nanoindentation measurements are performed along the out-of-plane direction to obtain the indentation modulus and hardness of BA_2PbI_4 crystals. The detailed measurement method can be found elsewhere[8]. The averaged indentation moduli of samples #1 and #2 are 4.37 ± 0.25 GPa and 4.32 ± 0.29 GPa, respectively, which are close to previously reported values ~3.62 GPa for analogous BA_2PbI_4 crystals[9]. However, they are much smaller than $MA_3Bi_2I_9$[8] (~12.4 GPa) and $MAPbI_3$[10–13] (~11.4 - 16.1 GPa) crystals, indicating a more compliant nature, likely due to lack of a continuous network of stiff inorganic bonds across layers in BA_2PbI_4 crystals. The ultralow indentation modulus measured along the out-of-plane direction of BA_2PbI_4 crystals is consistent with ultralow phonon group velocity along that direction based on equation $v = \sqrt{E/\rho}$. The hardness values of samples #1 and #2 are 0.32 ± 0.03 GPa and 0.41 ± 0.05 GPa, respectively, which are slightly larger than the previously reported value of ~0.29 GPa for BA_2PbI_4 crystals[9]

and smaller than the values reported for $MA_3Bi_2I_9$[8] (~0.47 GPa) and $MAPbI_3$[10] (~0.55 GPa) crystals. These results demonstrate that the BA_2PbI_4 crystals are softer than $MA_3Bi_2I_9$ and $MAPbI_3$ crystals.

IXS measurements

The IXS measurements are conducted on a single crystal with a size of $68\,\mu m \times 191\,\mu m \times 224\,\mu m$ at 300 K at beamline 30ID at the Advanced Photon Source (APS), Argonne National Laboratory. A full description of IXS at APS 30ID can be found in prior work[14]. The instrument operates at 23.7 keV. The instrument resolution is measured beforehand and an energy resolution of 1.5 meV is determined. Measured energy spectra are fitted with Lorentzian peaks convoluted with a pseudo-Voigt function to simulate instrument resolution. The measured acoustic phonon modes in the low Q regions are hard to resolve because of the strong elastic peak tail overwhelming the acoustic phonon excitations.

An example of the fitting curve is shown in Figure S8. Short acoustic phonon lifetimes of the BA_2PbI_4 single crystal from IXS measurements at 300 K are shown in Figure S9. They are mainly in the range of 0.5-30 ps. During the IXS measurements, we change the measurement spot after finishing each phonon branch in one direction to minimize the radiation damage. The determined lattice parameters remain the same until the measurements on the transverse modes along the Γ-Z direction, where we find a 0.5% change in the lattice parameters, indicating possible degradation. Therefore, we do not include the data for the transverse modes along the Γ-Z direction in the dispersion plot. For reported data, we think the radiation damage should be negligible.
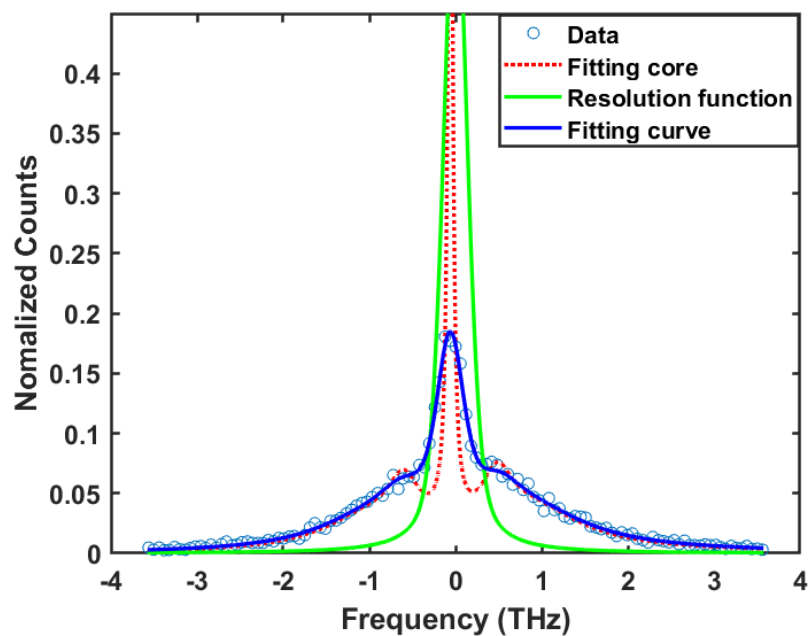
Figure S8. Energy spectra from IXS measurement (blue circles) of the LA mode at q=0.5 along [010] for the BA$_2$PbI$_4$ single crystals at 300 K characterized by an elastic peak centered at zero energy and inelastic peaks associated with the creation and annihilation of phonons. Green and red curves represent the instrumental resolution function and fitting core based on the Lorentzian function, respectively. The blue solid curve denotes the convolution between the resolution function and the fitting core.

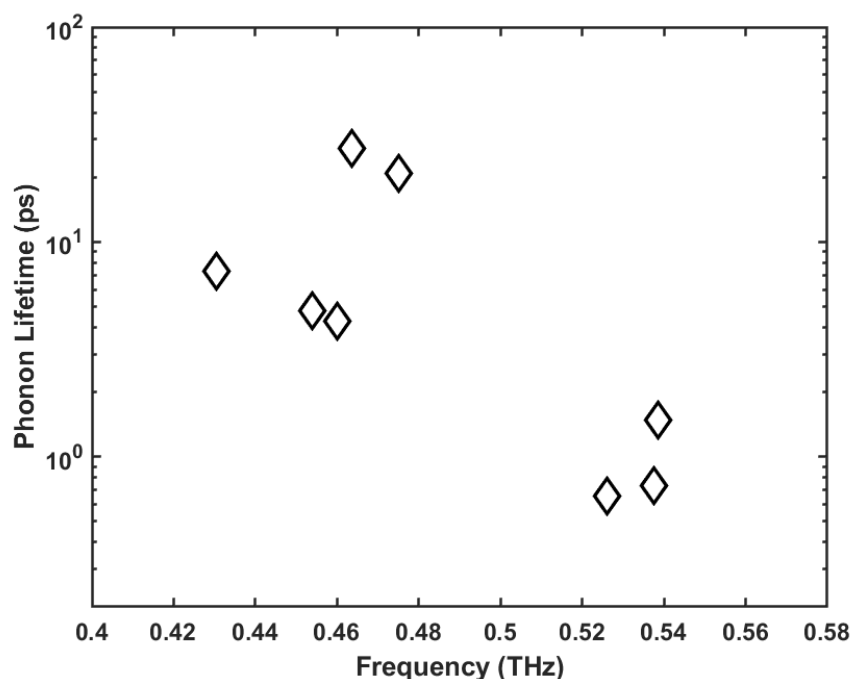**Figure S9.** Short acoustic phonon lifetimes of the BA_2PbI_4 single crystal from IXS measurements at 300 K. They are mainly in the range of 0.5-30 ps. Note that it is not a complete dataset of the full Brillouin zone.

EMD simulations

Interatomic forces for 2D BA_2PbI_4 are obtained by combining the MYP potential for 3D $MAPbI_3$[15] with the GAFF[16] force field for the organic alkylammonium molecules. The atomic charges of $C_4H_9NH_3^+$ molecules are calculated by the AM1-BCC method as implemented in the AMBER tools[17]. Charges of the Pb and I atoms are taken from MYP0 and a constant correction is applied to eventually neutralize the unit cell of the 2D crystal. The hybrid interactions are determined by Lorentz-Berthelot mixing rules of Lennard-Jones parameters from MYP0 and GAFF. The optimized lattice parameters of BA_2PbI_4 single crystal in MD simulations are listed in Table S2, in comparison with experimental values determined from SC-XRD.

Table S2. Crystal data and structure refinement for BA_2PbI_4 single crystal used in IXS measurements.

	a / Å	b / Å	c / Å	α	β	γ
MD simulations	8.8764	8.6925	27.6014	90°	90°	90°
Experiments	8.8810	8.6999	27.6251	90°	90°	90°

For the validation of MYP potential, we want to emphasize that the MYP potential is a non-harmonic potential based on a simple but physically sound description of ionic interactions in terms of long-range electrostatic forces, Buckingham and Lennard-Jones terms[18] that has been applied with success to study many properties of 3D hybrid perovskites showing transferability to non-bulk properties such as defects[19], surfaces and contact angles[20], water degradation[20] and thermal properties:

1) the model is able to reproduce the volume expansion with temperature (that is related to anharmonicity) of 3D hybrid perovskites and the corresponding phase transitions, including the temperature effects of the stochastic rotational dynamics of molecules in the different phases[21];

2) the model provides a reasonable description of vibrational properties of hybrid perovskites reproducing the broadening of vibrational peaks that are directly related to phonon interactions (anharmonicities);

3) the MYP potential has been already applied to calculate the thermal conductivity of 3D hybrid perovskites[22] providing results that are consistent with experimental results[23];

4) concerning 2D layers, vibrational density of states, mechanical constants and heat capacities calculated by the present model have been reported[24] and are in reasonable agreement with experiments and previous literature.

To further demonstrate that MYP potentials include the anharmonicities of 2D BA_2PbI_4 single crystal, we further calculate its Grüneisen parameter by equation (S3) using molecular dynamics simulations.

$$\gamma = \frac{1}{C_V}\left(\frac{\partial P}{\partial T}\right)_V \tag{S3}$$

where γ, C_V, P, and T are Grüneisen parameter, volumetric heat capacity, pressure and temperature of studied system, respectively[25]. The calculated pressure (P) as a function of temperature (T) of 2D BA_2PbI_4 single crystal are plotted in Figure S10 and we can get $\frac{\partial P}{\partial T} = 10.19\ (atm\ K^{-1})$. We know that $C_V = 0.48\ J\,g^{-1}K^{-1}$ for 2D BA_2PbI_4 single crystal. Then we plug these numbers into equation (S3) to extract $\gamma = 0.80$, which is comparable to the experimental Grüneisen parameters ($\gamma = 1.17$) of $CH_3NH_3PbI_3$[26].
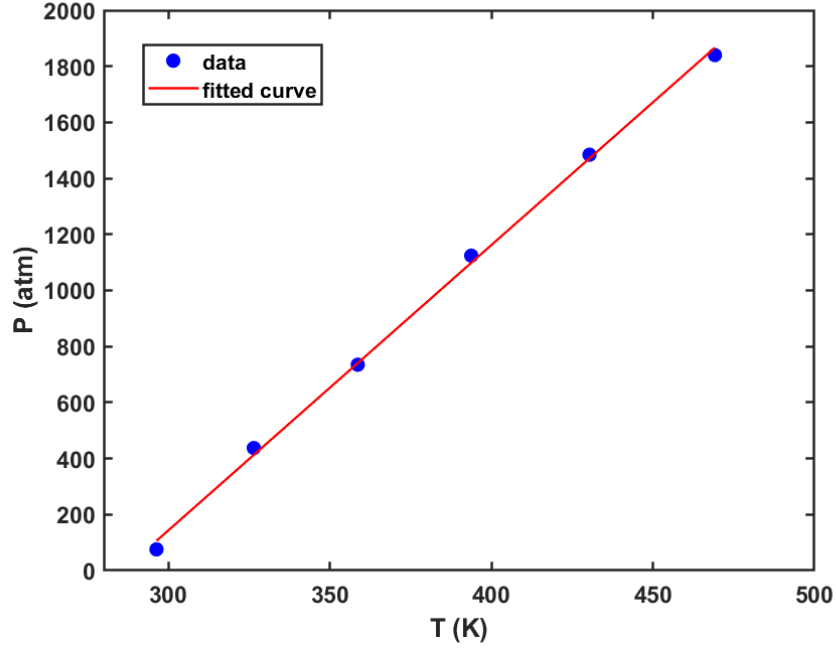
Figure S10. Pressure (P) as a function of temperature (T) of 2D BA$_2$PbI$_4$ single crystal calculated using molecular dynamics simulations. Blue dots are calculated data and red line is the linear fit with a slope=10.19.

The thermal conductivity (k) of 2D BA$_2$PbI$_4$ is calculated using the LAMMPS package[27]. 3×3×2 supercells are used to rule out the size effects. The timestep is set to 0.5 fs and periodic boundary conditions are applied in x, y, and z directions. The cutoff distance for both vdW and electrostatic interactions is 10 Å. In EMD simulations, k is determined from the autocorrelation of instantaneous heat flux through the Green-Kubo formula based on linear response theory[28–30]. The k is given by Equation (S4)

$$k_i(T) = \frac{1}{k_B T^2 V} \int_0^\infty \langle \vec{J}_i(t) \cdot \vec{J}_i(t+\tau) \rangle \, d\tau \tag{S4}$$

where k_i is the thermal conductivity along i direction, i.e. x, y, and z. V is the volume of the supercells, k_B is Boltzmann constant, T is the absolute temperature, τ is the delay time. We first

16

relax the system in canonical (NVT) and microcanonical (NVE) ensembles subsequently for 400

ps and 200 ps in each ensemble before collecting heat flux data in an NVE ensemble for another

0.5 ns. All *k's* are averaged over 10 different ensembles.

SED Method

The SED method is used to calculate phonon dispersions. SED is defined by

$$\Phi(q, \omega) = \frac{1}{4\tau_0\pi} \sum_\alpha \sum_b^B \frac{m_b}{N} \left| \int_0^{\tau_0} \sum_l^N \dot{u}_\alpha \left(\begin{matrix} l \\ b \end{matrix}, t \right) exp(iq * r_l - i\omega t) \, dt \right|^2 \tag{S5}$$

where q is the wave vector, ω is the wave frequency, α represents integration directions (x, y,

z), τ_0 is the integration time, N is the total number of unit cells in the simulated supercell, B is the

total number of atoms in a unit cell, m_b is the mass of atom b in the unit cell, $\dot{u}_\alpha \left(\begin{matrix} l \\ b \end{matrix}, t \right)$ is the α-th

component of velocity of atom b in cell l, and r_l is the equilibrium positon of cell l. Atomic

velocities of all atoms in the supercells are collected every 10 fs during an NVE ensemble for 100

ps. The phonon dispersion along **Γ-X, Γ-Y,** and **Γ-Z** directions at 300K is calculated by the 2D

Fourier transform of each $\dot{u}_\alpha$ and r_l combination as shown in Equation (S5). 20×20×1 and 1×1×20

supercells are used to calculate phonon dispersion along **Γ-X/Y** and **Γ-Z** directions, respectively.

Phonon Dispersion Analysis

Similar to layered graphite, Figure 3a shows three distinguishable acoustic branches along **Γ-X** or

Γ-Y directions: the longitudinal acoustic (LA), the in-plane transverse acoustic (TA) mode, and

the out-of-plane z-axis acoustic (ZA) mode; there are one LA and two degenerate TA modes in

the **Γ-Z** direction. The phonon dispersion along **Γ-X** direction is similar to that along **Γ-Y** direction

due to the structural similarities in the two directions. The calculated phonon dispersion from SED

match well with the measured phonon modes near the zone boundaries.

The phonon dispersion of BA_2PbI_4 (Figure 3a) shows that the acoustic phonon modes have ultralow frequencies of up to ~0.55 THz along the in-plane direction (**Γ-X** and **Γ-Y**) and up to ~0.4 THz along the out-of-plane direction (**Γ-Z**). They are even lower than the previously reported lowest phonon frequency of the "0D" hybrids $MA_3Bi_2I_9$ (~0.7 THz)[8]. These ultralow acoustic modes lead to small phonon group velocities, which are critical to the ultralow thermal conductivity of BA_2PbI_4 crystals. Moreover, there is a significant overlap between acoustic and optical branches along all the high symmetry lines, as previously observed in other hybrid organic-inorganic crystals[8,31]. The significant overlap could result in strong acoustic-optical phonon scattering and correspondingly short phonon lifetimes, as shown in Figure S9, thereby contributing to the ultralow thermal conductivity.

Phonon lifetimes

We estimate phonon lifetimes along in-plane (Γ-X/Y) and out-of-plane directions (Γ-Z) by fitting each SED peak with the Lorentzian or Gaussian function. We plot 1/FWHM as a function of their frequencies, as shown in Figure S11. Despite a rough estimation, a general trend can be observed that phonon lifetimes along the in-plane direction (blue spheres) are slightly larger than that along the in-plane direction (red spheres). We cannot make a direct comparison between the calculated phonon lifetimes with our measured ones from IXS because of the following reasons: 1) Small supercell (20×20×1) in the SED calculation leads to low resolution for the peaks and the fitting quality is low. 2) Our calculated directions (Γ-X: (X 0.05 0) Γ-Y: (0.05 Y 0)) are not exactly along high symmetric lines ((Γ-X: (X 0 0) Γ-Y: (0 Y 0)). Nevertheless, we feel reasonably confident to argue that the in-plane phonon lifetimes tend to be larger because these calculations were performed consistently. Note that although the peak widths from SED calculations cannot be directly treated as the phonon lifetimes, it does not affect the thermal conductivity calculation

because we calculate the thermal conductivity from a completely separate procedure based on the linear response theory, and the values are not limited by the SED resolution.
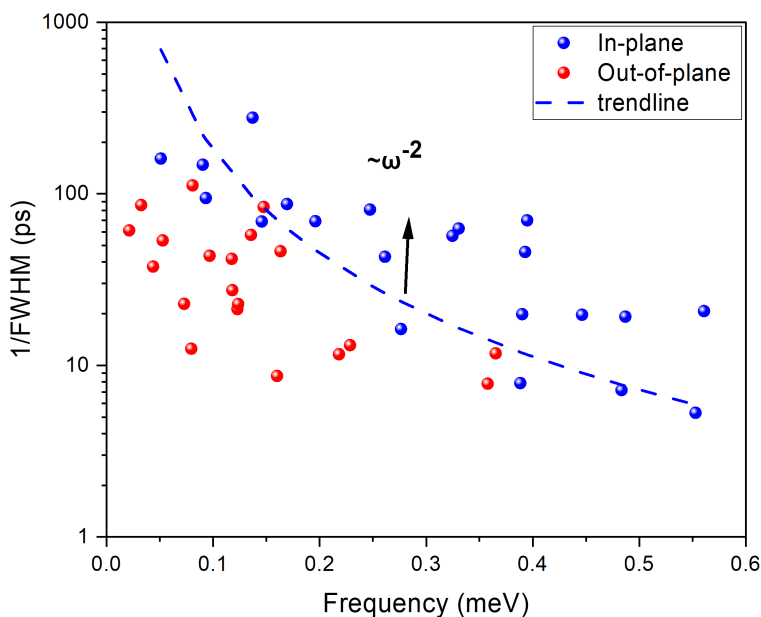

Figure S11. Inverse of FWHM of SED peaks as a function of their corresponding frequencies for 2D BA$_2$PbI$_4$ single crystal. Note that this calculation is based on 20×20×1 supercell and along in-plane: Γ-X: (X 0.05 0) and Γ-Y: (0.05 Y 0); out-of-plane: Γ-Z: (0 0 Z).

Phonon group velocity

We calculate the acoustic phonon group velocities from the slope of LA/TA branches at **Γ** point based on SED as in Table S3. The overall phonon group velocity along the in-plane direction in BA$_2$PbI$_4$ is even 15.0% smaller than that along the out-of-plane direction, which is quite different from graphite, which shows large anisotropy in the thermal conductivity since the in-plane phonon group velocities are significantly larger than the out-of-plane phonon group velocities[32].

We can only measure the acoustic phonon modes near the zone boundaries by IXS because the acoustic phonon frequencies of BA_2PbI_4 near Γ point are too low and below the energy resolution of the IXS technique. We use pulse echo technique to perform the speed of sound measurements on sample #1 to support the low frequency phonon modes near Γ point.

Pulse echo ultrasound, in which short bursts of ultrasound are excited and detected in a sample using a piezoelectric transducer, provides a direct measurement of the speed of sound. The sample is prepared with two opposing, flat, parallel faces, and a compressional transducer (Boston Piezo-Optics Y-cut lithium niobate) is fixed to one face of the sample with a thin layer of epoxy (AngstromBond 9110LV). The transducer is excited with a pulse of RF voltage, and the resulting strain wave propagates through the sample. After being reflected off the opposing face, the pulse returns to the transducer, where it is detected as an RF voltage via the inverse piezoelectric effect. The strain wave continues to bounce between the sample's faces producing a decaying series of voltage echoes which are recorded on a digital oscilloscope. The spacing between successive echoes, combined with knowledge of the sample's thickness, can be used to determine the absolute value of the speed of sound in the sample.

Figure S12 shows the echo pattern with a 242 MHz excitation and a 50 ns pulse width, along with the component of the signal at the drive frequency, obtained by digital lock-in. Though clear peaks are visible in the signal, the echo pattern contains extra features, most likely due to stray reflections and interaction between the ultrasonic wave and the epoxy used to bond the transducer to the sample. Identifying the peak positions is further complicated by interference between the stray reflections and the echoes. However, distinct sets of peaks, one of which is highlighted in Figure S12, are present with a spacing of 280 ± 30 ns corresponding to a speed of sound of 1400 ± 100 m/s.
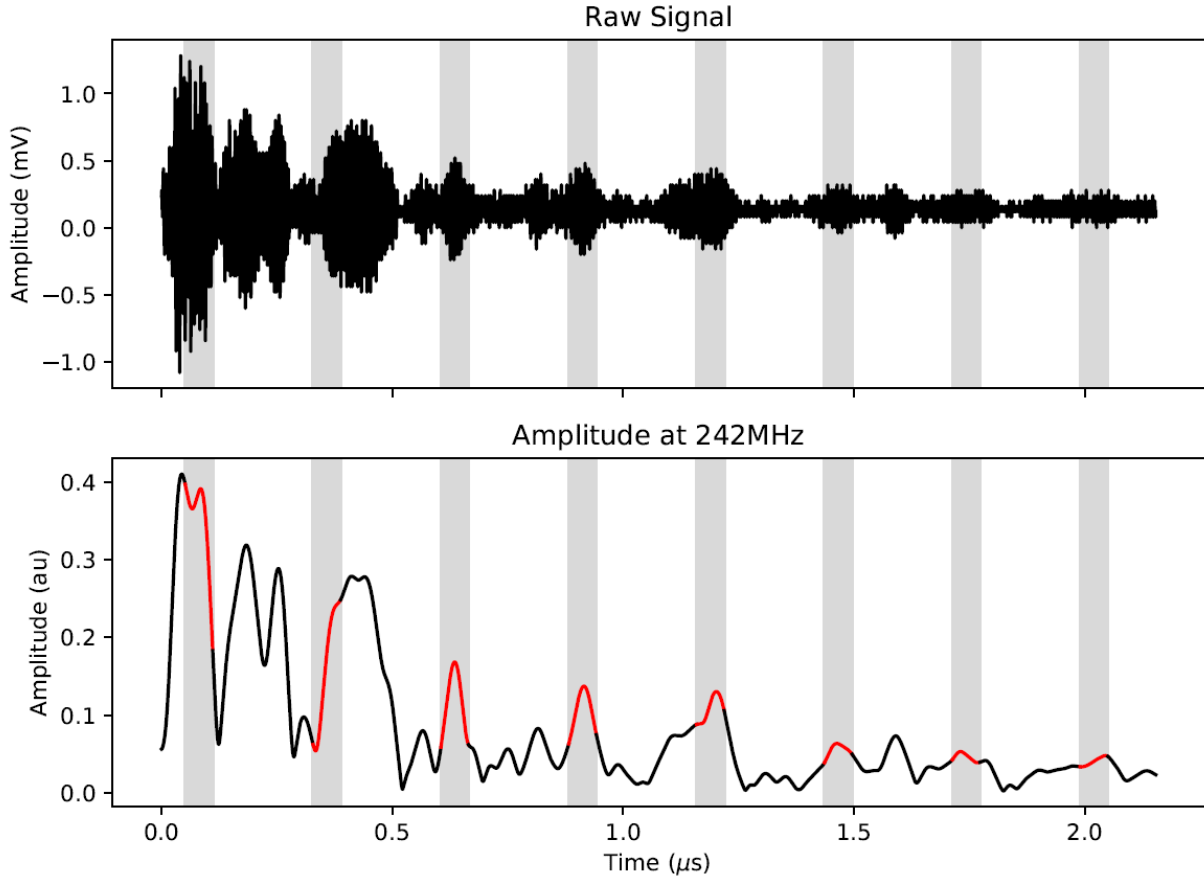
Figure S12. The pulse echo signal of suspended BA_2PbI_4 crystal with a thickness of 0.19 mm. Distinct sets of peaks, which are highlighted, are present with a spacing of 280 ± 30 ns corresponding to a speed of sound of 1400 ± 100 m/s.

We could also estimate the speed of sound from the nanoindentation measurements via $v_{LA} = \sqrt{\frac{B+4/3G}{\rho}}$ and $v_{TA} = \sqrt{\frac{G}{\rho}}$, where B is the bulk modulus and G is the shear modulus. The measured indentation moduli E_{ind} of samples #1 and #2 are 4.37 ± 0.25 GPa and 4.32 ± 0.29 GPa, respectively. The Young's modulus is calculated as $E = E_{ind}(1 - v^2)$, where v is the Poisson ratio and we use its value of 0.29 in previous MD simulations[24]. The bulk modulus is obtained as $B =$

$\frac{E}{3(1-2v)}$, and the shear modulus is calculated as $G = \frac{E}{2(1+v)}$. Then we extract experimental acoustic

phonon group velocities as in Table S3.

Table S3. Acoustic phonon group velocities of BA_2PbI_4 based on phonon dispersion calculations

by SED, nanoindentation measurements, and pulse echo measurements.

Method	Direction	$v_{LA}(m/s)$	$v_{TA}(m/s)$	$v_{ZA}(m/s)$	$\bar{v}(m/s)$
SED calculations	[100]	1355	1110	147	871
	[010]	1415	1087	156	886
	[001]	1628	737		1034
Nanoindentation (sample #1)	[001]	1397 ± 40	760 ± 22		972 ± 28
Nanoindentation (sample #2)	[001]	1391 ± 47	757 ± 25		968 ± 32
Pulse echo (sample #1)	[001]	1400 ± 100			

Though not high-quality enough to be a conclusive measurement of the speed of sound on their

own, the pulse echo results are consistent with the nanoindentation measurements. We are thus

fairly confident that the speed of sound in [001] direction should be around 1400 m/s. We were

unable to measure the in-plane speed of sound because it requires parallel surfaces and our crystal

geometry does not satisfy that. The calculated longitudinal acoustic phonon group velocity (v_{LA})

along [001] direction is 1628 m/s, which is slightly larger than the experimental values (~1400

m/s). We think the possible reasons are 1) our calculated directions (Γ-X: (X 0.05 0) Γ-Y: (0.05 Y

0)) from 2D Fourier transform of the velocity field are a bit off from high symmetric lines ((Γ-X:

(X 0 0) Γ-Y: (0 Y 0)). If we have a large enough supercell, it will approach the high symmetry

lines. But we cannot afford the SED calculations based on a larger supercell because of the

complicated structure with 156 atoms in the unit cell. 2) Small supercell (20×20×1) in the SED

calculation leads to relatively low resolution in momentum space and causes uncertainties in phonon group velocities.

Bond strength estimation

We use the parallel model and series model to roughly estimate the effective bond energy in the in-plane and out-of-plane directions as in Figure S13, assuming the organic chains are straight chains in the out-of-plane direction. For the in-plane direction, we use the simplified model $E_{\parallel} = V_{org}E_{org,\parallel} + V_{inorg}E_{inorg,\parallel}$ where V_{org} =78% is the volume fraction of organic layers and V_{inorg}=22% is the volumetric fraction of inorganic layers, $E_{org,\parallel}$ is the effective bond energy of organic layers interactions in the in-plane direction, which is mainly from the interchain van der Waals interactions, and $E_{inorg,\parallel}$ is the bond energy of inorganic layers in the in-plane direction, we estimate the effective in-plane bond energy to be 34.4 kJ/mol per cell. The out-of-plane bond energy is calculated to be 32.1 kJ/mol by the simplified model $E_{\perp} = 1/[V_{org}/E_{org,\perp} + V_{inorg}/E_{inorg,\perp} + V_{electro}/E_{\text{electro},\perp} + V_{vdw}/E_{vdw,\perp})]$, where $V_{electro}$ and V_{vdw} are the volume fractions of electrostatic interactions and van der Waals interactions and we use the value of 5% for both. The estimated out-of-plane bond energy is comparable to the in-plane bond energy, as indicated by the comparable acoustic phonon group velocities between the in-plane and out-of-plane directions.
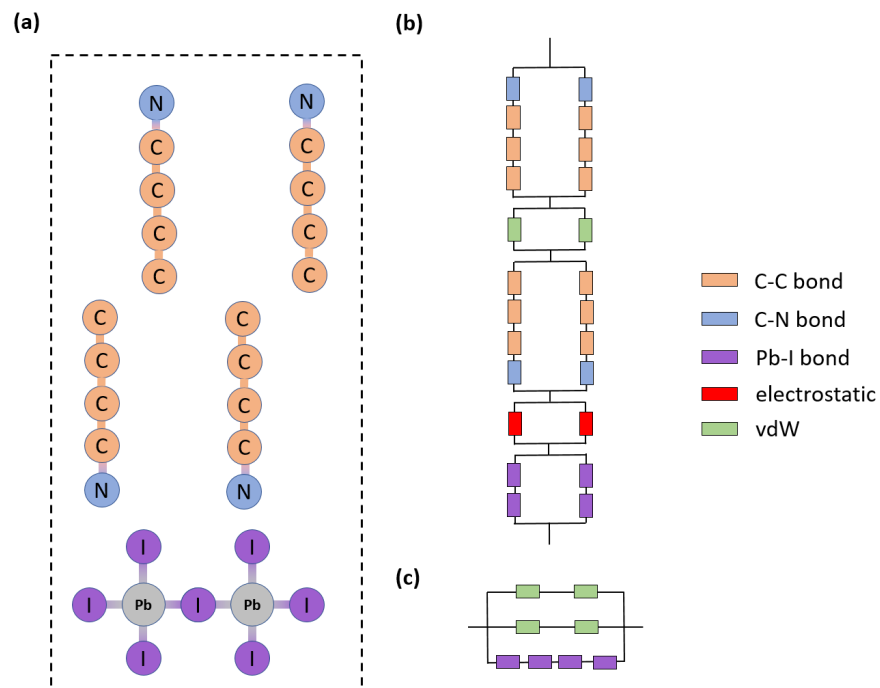
Figure S13. The simplified models for effective bond strength of BA_2PbI_4. (a) The simplified schematic of the BA_2PbI_4 cell. (b) The out-of-plane model for effective bond energy. (c) The in-plane model for effective bond energy.

REFERENCES

(1)   Billing, D. G.; Lemmerer, A. Synthesis, Characterization and Phase Transitions in the Inorganic–Organic Layered Perovskite-Type Hybrids [(CnH2n+ 1NH3) 2PbI4], N= 4, 5 and 6. *Acta Crystallogr. Sect. B Struct. Sci.* **2007**, *63* (5), 735–747.

(2)   Mitzi, D. B. Synthesis, Crystal Structure, and Optical and Thermal Properties of (C4H9NH3) 2MI4 (M= Ge, Sn, Pb). *Chem. Mater.* **1996**, *8* (3), 791–800.

(3)   Dolomanov, O. V; Bourhis, L. J.; Gildea, R. J.; Howard, J. A. K.; Puschmann, H. OLEX2: A Complete Structure Solution, Refinement and Analysis Program. *J. Appl. Crystallogr.*

2009, *42* (2), 339–341.

(4) Sheldrick, G. M. SHELXT–Integrated Space-Group and Crystal-Structure Determination. *Acta Crystallogr. Sect. A Found. Adv.* **2015**, *71* (1), 3–8.

(5) Johnson, J. A.; Maznev, A. A.; Bulsara, M. T.; Fitzgerald, E. A.; Harman, T. C.; Calawa, S.; Vineis, C. J.; Turner, G.; Nelson, K. A. Phase-Controlled, Heterodyne Laser-Induced Transient Grating Measurements of Thermal Transport Properties in Opaque Material. *J. Appl. Phys.* **2012**, *111* (2), 23503.

(6) Johnson, J. A.; Maznev, A. A.; Cuffe, J.; Eliason, J. K.; Minnich, A. J.; Kehoe, T.; Torres, C. M. S.; Chen, G.; Nelson, K. A. Direct Measurement of Room-Temperature Nondiffusive Thermal Transport Over Micron Distances in a Silicon Membrane. *Phys. Rev. Lett.* **2013**, *110* (2). https://doi.org/10.1103/PhysRevLett.110.025901.

(7) Li, C.; Ma, Y.; Tian, Z. Thermal Switching of Thermoresponsive Polymer Aqueous Solutions. *ACS Macro Lett.* **2017**, 53–58. https://doi.org/10.1021/acsmacrolett.7b00938.

(8) Ma, H.; Li, C.; Ma, Y.; Wang, H.; Rouse, Z. W.; Zhang, Z.; Slebodnick, C.; Alatas, A.; Baker, S. P.; Urban, J. J. Supercompliant and Soft (CH 3 NH 3) 3 Bi 2 I 9 Crystal with Ultralow Thermal Conductivity. *Phys. Rev. Lett.* **2019**, *123* (15), 155901.

(9) Tu, Q.; Spanopoulos, I.; Hao, S.; Wolverton, C.; Kanatzidis, M. G.; Shekhawat, G. S.; Dravid, V. P. Out-of-Plane Mechanical Properties of 2D Hybrid Organic-Inorganic Perovskites by Nanoindentation. *ACS Appl. Mater. Interfaces* **2018**, *10* (26), 22167–22173. https://doi.org/10.1021/acsami.8b05138.

(10) Rakita, Y.; Cohen, S. R.; Kedem, N. K.; Hodes, G.; Cahen, D. Mechanical Properties of

APbX3 (A = Cs or CH3NH3; X = i or Br) Perovskite Single Crystals. *MRS Commun.*
2015, *5* (4), 623–629. https://doi.org/10.1557/mrc.2015.69.

(11)   Sun, S.; Fang, Y.; Kieslich, G.; White, T. J.; Cheetham, A. K. Mechanical Properties of
       Organic-Inorganic Halide Perovskites, CH3NH3PbX3 (X = I, Br and Cl), by
       Nanoindentation. *J. Mater. Chem. A* **2015**, *3* (36), 18450–18455.
       https://doi.org/10.1039/c5ta03331d.

(12)   Park, M.; Kim, H. J.; Jeong, I.; Lee, J.; Lee, H.; Son, H. J.; Kim, D. E.; Ko, M. J.
       Mechanically Recoverable and Highly Efficient Perovskite Solar Cells: Investigation of
       Intrinsic Flexibility of Organic-Inorganic Perovskite. *Adv. Energy Mater.* **2015**, *5* (22), 1–
       11. https://doi.org/10.1002/aenm.201501406.

(13)   Elbaz, G. A.; Ong, W. L.; Doud, E. A.; Kim, P.; Paley, D. W.; Roy, X.; Malen, J. A.
       Phonon Speed, Not Scattering, Differentiates Thermal Transport in Lead Halide
       Perovskites. *Nano Lett.* **2017**, *17* (9), 5734–5739.
       https://doi.org/10.1021/acs.nanolett.7b02696.

(14)   Said, A. H.; Sinn, H.; Toellner, T. S.; Alp, E. E.; Gog, T.; Leu, B. M.; Bean, S.; Alatas, A.
       High-Energy-Resolution Inelastic X-Ray Scattering Spectrometer at Beamline 30-ID of
       the Advanced Photon Source. *J. Synchrotron Radiat.* **2020**, *27* (3).

(15)   Mattoni, A.; Filippetti, A.; Saba, M. I.; Delugas, P. Methylammonium Rotational
       Dynamics in Lead Halide Perovskite by Classical Molecular Dynamics: The Role of
       Temperature. *J. Phys. Chem. C* **2015**, *119* (30), 17421–17428.

(16)   Wang, J.; Wolf, R. M.; Caldwell, J. W.; Kollman, P. A.; Case, D. A. Development and

Testing of a General Amber Force Field. *J. Comput. Chem.* **2004**, *25* (9), 1157–1174.

(17) Case, D. A.; Cheatham III, T. E.; Darden, T.; Gohlke, H.; Luo, R.; Merz Jr, K. M.; Onufriev, A.; Simmerling, C.; Wang, B.; Woods, R. J. The Amber Biomolecular Simulation Programs. *J. Comput. Chem.* **2005**, *26* (16), 1668–1688.

(18) Mattoni, A.; Filippetti, A.; Caddeo, C. Modeling Hybrid Perovskites by Molecular Dynamics. *J. Phys. Condens. Matter* **2016**, *29* (4), 43001.

(19) Delugas, P.; Caddeo, C.; Filippetti, A.; Mattoni, A. Thermally Activated Point Defect Diffusion in Methylammonium Lead Trihalide: Anisotropic and Ultrahigh Mobility of Iodine. *J. Phys. Chem. Lett.* **2016**, *7* (13), 2356–2361.

(20) Caddeo, C.; Marongiu, D.; Meloni, S.; Filippetti, A.; Quochi, F.; Saba, M.; Mattoni, A. Hydrophilicity and Water Contact Angle on Methylammonium Lead Iodide. *Adv. Mater. Interfaces* **2019**, *6* (3), 1801173.

(21) Onoda-Yamamuro, N.; Yamamuro, O.; Matsuo, T.; Suga, H. PT Phase Relations of CH3NH3PbX3 (X= Cl, Br, I) Crystals. *J. Phys. Chem. Solids* **1992**, *53* (2), 277–281.

(22) Caddeo, C.; Melis, C.; Saba, M. I.; Filippetti, A.; Colombo, L.; Mattoni, A. Tuning the Thermal Conductivity of Methylammonium Lead Halide by the Molecular Substructure. *Phys. Chem. Chem. Phys.* **2016**, *18* (35), 24318–24324.

(23) Wang, M.; Lin, S. Anisotropic and Ultralow Phonon Thermal Transport in Organic–Inorganic Hybrid Perovskites: Atomistic Insights into Solar Cell Thermal Management and Thermoelectric Energy Conversion Efficiency. *Adv. Funct. Mater.* **2016**, *26* (29), 5297–5306.

(24)   Giri, A.; Chen, A. Z.; Mattoni, A.; Aryana, K.; Zhang, D.; Hu, X.; Lee, S.-H.; Choi, J. J.; Hopkins, P. E. Ultralow Thermal Conductivity of Two-Dimensional Metal Halide Perovskites. *Nano Lett.* **2020**.

(25)   Stevenson, C. S.; Curro, J. G.; McCoy, J. D. Gruneisen Parameters of Bead-Spring Chains: MD Simulation and Theory. *J. Chem. Phys.* **2020**, *153* (24), 244903.

(26)   Ge, C.; Hu, M.; Wu, P.; Tan, Q.; Chen, Z.; Wang, Y.; Shi, J.; Feng, J. Ultralow Thermal Conductivity and Ultrahigh Thermal Expansion of Single-Crystal Organic-Inorganic Hybrid Perovskite $CH_3NH_3PbX_3$ (X = Cl, Br, I). *J. Phys. Chem. C* **2018**, *122* (28), 15973–15978. https://doi.org/10.1021/acs.jpcc.8b05919.

(27)   Plimpton, S. Fast Parallel Algorithms for Short-Range Molecular Dynamics. *J. Comput. Phys.* **1995**, *117* (1), 1–19.

(28)   Green, M. S. Markoff Random Processes and the Statistical Mechanics of Time-Dependent Phenomena. II. Irreversible Processes in Fluids. *J. Chem. Phys.* **1954**, *22* (3), 398–413. https://doi.org/doi:http://dx.doi.org/10.1063/1.1740082.

(29)   Green, M. S. Markoff Random Processes and the Statistical Mechanics of Time-Dependent Phenomena. *J. Chem. Phys.* **1952**, *20* (8), 1281–1295. https://doi.org/doi:http://dx.doi.org/10.1063/1.1700722.

(30)   Babaei, H.; Keblinski, P.; Khodadadi, J. M. Equilibrium Molecular Dynamics Determination of Thermal Conductivity for Multi-Component Systems. *J. Appl. Phys.* **2012**, *112* (5), 54310.

(31)   Ma, H.; Ma, Y.; Wang, H.; Slebodnick, C.; Alatas, A.; Urban, J. J.; Tian, Z. Experimental

Phonon Dispersion and Lifetimes of Tetragonal CH3NH3PbI3 Perovskite Crystals. *J. Phys. Chem. Lett.* **2018**, *10* (1), 1–6.

(32)   Alofi, A. S. S. Theory of Phonon Thermal Transport in Graphene and Graphite. **2014**.